Stresses at the Cell-to-Substrate Interface during Locomotion of Fibroblasts

Micah Dembo* and Yu-Li Wang#

*Department of Biomedical Engineering, Boston University, Boston, Massachusetts 02215-2407, and #Department of Physiology, University of Massachusetts Medical School, Worcester, Massachusetts 01605

ABSTRACT Recent technological improvements in the elastic substrate method make it possible to produce spatially resolved measurements of the tractions exerted by single motile cells. In this study we have applied these developments to produce maps of the tractions exerted by 3T3 fibroblasts during steady locomotion. The resulting images have a spatial resolution of ~5 μm and a maximum intensity of ~10^2 kdyn/cm^2 (10^4 pN/μm^2). We find that the propulsive thrust for fibroblast locomotion, ~0.2 dyn, is imparted to the substratum within 15 μm of the leading edge. These observations demonstrate that the lamellipodium of the fibroblast is able to generate intense traction stress. The cell body and posterior seem to be mechanically passive structures pulled forward entirely by this action.

INTRODUCTION

Various studies have suggested that mechanical stress exerted at cell-substratum and cell-cell interfacial boundaries is involved in the effectuation and regulation of a variety of physiological processes. These include many types of ameboid motion (Cramer and Mitchison, 1993; Condeelis, 1993; Oliver et al., 1994; Sheetz, 1994), the anchorage dependency of growth control (Chen et al., 1997; Chrzanowska-Wodnicka and Burridge, 1996; Folkman and Moscona, 1978), and the remodeling of extracellular matrix (Barocas and Tranquillo, 1997). The elastic substrate method is one of the few existing approaches that can yield direct quantitative information about the detailed magnitude, direction, and location of such interfacial stresses.

The basic idea of using an elastic substrate to study the forces produced by single cells was originally conceived by Harris and co-workers (Harris et al., 1980; Harris, 1988). Harris-type substrata are produced by inducing polymerization of a very thin film on the surface of liquid silicone. In many cases cellular tractions cause such a film to buckle, and the consequent wrinkle field then provides a highly visible semiquantitative readout of mechanical action. A recent application of wrinkling film technology is described by Burton and Taylor (1997). Unfortunately, wrinkles in silicone substrata are usually larger than the cells generating them. In addition, the wrinkles develop very slowly and are intrinsically nonlinear and chaotic. These characteristics severely limit the spatial and temporal resolution of the technique.

A means of constructing nonwrinkling elastic substrata was first discovered in an empirical fashion by Lee et al. (1994). The method is identical to that used by Harris except that during polymerization the edges of the film become welded to the sides of a rigid vessel (Oliver et al., 1998). After the polymerization step, conditions are changed so that the film spontaneously shrinks and stretches tightly, like a drumhead. Because of the tight tension, wrinkling modes are suppressed even though the substratum is still elastic and still free to undergo in-plane shearing deformations. These are detected as movements of embedded marker beads.

In the case of fish epidermal keratocytes (small rapidly motile cells from the scale), prestressed silicone films have been successfully used to obtain high-resolution traction images (Oliver et al., 1995; Dembo et al., 1996). However, no one has successfully devised a nonwrinkling silicone substratum for studies of cultured mammalian cells. This is mainly because it is difficult to "tune" the mechanical properties of silicone rubber films to match the strength and motility rate of such cells.

The disadvantages of silicone substrata have recently been overcome by the introduction of polyacrylamide substrata (Pelham and Wang, 1997; Wang and Pelham, 1998). The added benefit of polyacrylamide is that its stiffness can be readily adjusted by controlled variations of the monomer and cross-linker concentrations. Thus, regardless of the stresses produced by a particular cell type, trial and error usually allows production of a material that will undergo controlled linear deformations of a detectable magnitude.

In the case of 3T3 fibroblasts, preliminary studies have indicated satisfactory performance with films consisting of 10% acrylamide and 0.03% bis-acrylamide (Pelham and Wang, 1997; Wang and Pelham, 1998). For our present purposes, this standard "fibroblast substratum" is deposited in a layer ~70 μm in thickness covalently bonded on the lower surface to a glass coverslip. Fluorescent latex marker beads are embedded randomly throughout the polyacrylamide so that deformations can be easily visualized (the beads we use are 0.2 μm in diameter). Finally, the exposed surface of the polyacrylamide substrata is covalently decorated with an extracellular matrix protein (type I collagen).

Received for publication 3 August 1998 and in final form 25 January 1999.

Address reprint requests to M. Dembo, Dept. of Biomedical Engineering, 44 Cummington Street, Boston, MA 02215-2407. Tel.: 617-353-1671; Fax: 617-353-6766; E-mail: mxd@bu.edu.

0006-3495/99/04/2307/10 $2.00

METHODS

Preparation of activated glass coverslips

Coverslips were chemically activated to allow stable, covalent association of polyacrylamide sheets: 1) coverslips (No. 1, 45 mm × 50 mm; Fisher Scientific, Pittsburgh, PA) were passed briefly through the inner flame of a Bunsen burner. 2) A drop of 0.1 N NaOH was smeared over the surface of each coverslip with a Pasteur pipette and allowed to dry in air. 3) The treated side of the coverslips was marked using a diamond-tipped pen and a small drop of 3-aminopropyltrimethoxysilane (Sigma, St. Louis, MO) was smeared evenly on this surface. 4) After 4–5 min the coverslips were washed extensively with distilled H_2O. 5) The coverslips were then transferred, marked-side up, into petri dishes and covered with 0.5% glutaraldehyde in PBS (prepared by diluting 1 part of 70% stock solution, Polysciences, Inc., Warrington, PA, with 140 parts of PBS). 6) After incubation at room temperature for 30 min the coverslips were washed extensively with multiple changes of distilled H_2O on a shaker and allowed to dry in air. 7) The treated coverslips were stored for up to 48 h after preparation.

Preparation of polyacrylamide sheets

Thin sheets of polyacrylamide gel were prepared and bonded to the activated glass surface of the coverslips: 1) acrylamide (Bio-Rad, Hercules, CA, 30% w/v) was mixed with *N*, *N*-methylene-bis-acrylamide (BIS, Bio-Rad, 2.5% w/v) and distilled H_2O to obtain a final concentration of 10% acrylamide and 0.03% BIS. For more rigid or more flexible substrata the percentage of BIS was increased or decreased. 2) Fluorescent latex beads (0.2 μm FluoSpheres, carboxylate-modified, Cat. No. F-8821 or equivalent, Molecular Probes, Eugene, OR) were sonicated briefly in a bath sonicator and added to the acrylamide mixture in volume ratio of 1:125. 3) The acrylamide/BIS solution was degassed and polymerization was initiated by addition of ammonium persulfate (10% w/v solution, Bio-Rad, 1:200 volume) and *N*,*N*,*N*,*N*-tetramethyl ethylenediamine (TEMED, Bio-Rad, 1:2000 volume). 4) Twenty-five μl of the acrylamide solution was immediately placed onto the surface of an activated coverslip and the droplet was flattened using a large circular coverslip (No. 1, 22 mm diam., Fisher). 5) The resulting sandwich assembly was turned upside down. 6) After polymerization (10–30 min), the circular cover glass was removed and the gel was washed on a shaker with HEPES (50 mM, pH 8.5).

Conjugation of collagen to the polyacrylamide surface

To provide a physiological surface for cell culture, a saturating density of type I collagen was covalently attached to the base surface of the acrylamide gel. We accomplish this using a photoactivatable heterobifunctional reagent called sulfo-SANPAH (sulfosuccinimidyl 6 (4-azido-2-nitrophenyl-amino) hexanoate). This compound contains a succinimidyl ester group that will react with the lysine ε-NH_2 moieties of proteins and also a phenylazide group that, upon photoactivation, reacts nonspecifically with many chemically inert molecules including polyacrylamide and water. The detailed procedure follows: 1) fluid was drained off the surface of the polyacrylamide gels and 200 μl of Sulfo-SANPAH (1 mM in 50 mM HEPES, pH 8.5, Pierce Chemicals, Rockford, IL) was applied. 2) The surface of each gel was then exposed to UV light from a 30 W germicidal lamp at a distance of 6 inches for 5 min. The darkened Sulfo-SANPAH solution was removed and the photoactivation procedure was repeated a second time. 3) The glass-supported polyacrylamide sheets were twice subjected to 15 min shaker washes with 50 mM HEPES (pH 8.5). 4) The polyacrylamide sheets were then covered with a solution of soluble type I collagen (0.2 mg/ml, Amersham Life Science, Arlington Heights, IL) and allowed to react overnight at 4°C on a shaker. 5) The gels were then washed extensively with PBS, mounted onto culture chambers, and sterilized with UV irradiation.

Cell culture

Before plating cells, gels were soaked for 30–45 min in culture medium at 37°C. Swiss 3T3 cells (American Type Culture Collection, Rockville, MD) were cultured in DMEM (Sigma, St. Louis, MO) supplemented with 10% donor calf serum (JHR Biosciences, Lenexa, KS), 2 mM L-glutamine, 50 μg/ml streptomycin, 50 U/ml penicillin, and 250 ηg/ml amphotercin B (Gibco-BRL, Gaithersburg, MD).

Microscopy

Phase images of cells and fluorescence of substrate-embedded beads were recorded simultaneously with a Zeiss 40×, NA 0.65 Achromat phase objective on a Zeiss IM-35 microscope. The depth of the field was ~5 μm. All images were recorded with a cooled CCD camera (TE/CCD-576EM; Princeton Instruments, Trenton, NJ or CH250, Photometrics, Tucson, AZ) and processed for background subtraction.

Characterization of substrata

The thickness of the substrate was estimated by the initial volume of the acrylamide solution applied to the coverslip and the area of the gel. The actual thickness was measured by focusing a microscope from the glass surface up to the gel surface. The thickness was affected by the acrylamide/BIS concentration and by the degree of swelling of the gel in media. The protocol above gives a gel ~70 μm in thickness.

To measure Young's modulus, a large coverslip was placed on top of a gel sheet so that the polyacrylamide was sandwiched between glass surfaces. The gel was submerged in culture medium so as to maintain constant hydration. Then small metal weights were used to apply a compressive force on the upper glass surface. The degree of compression was determined with the microscope focusing mechanism. Young's modulus for polyacrylamide gels was calculated using the formula; $E = (F/A)(L/\Delta L)$ where A = gel area, F = force, L = unstressed thickness, ΔL = change in gel thickness.

Young's modulus of the standard substratum used for traction imaging in this study (0.03% bis-acrylamide) was found to be 62 ± 1 kdyn/cm^2 (=6200 pN/μm^2). Substrata prepared using 0.24% bis-acrylamide were much stiffer than the standard material (~10^3 kdyn/cm^2). Within experimental uncertainty, these results are identical to those previously reported using a stretch test (Pelham and Wang, 1997; Wang and Pelham, 1998). Qualitatively, our fibroblast substrata are ~3 orders of magnitude softer than a typical sample of silicone rubber tubing.

We were unable to detect any changes in the total volume of gels during compression. This indicates that the Poisson ratio for polyacrylamide substrata is close to 0.5. The mechanical properties of our substrata were also probed microscopically with a microneedle and macroscopically by stretching strips with known weights. The response to stress was linear and recovery after strain was instantaneous. Even after 24 h of 30% strain, the gels recovered to their original dimensions (Pelham and Wang, 1997).

The relative (but not the absolute) amounts of collagen on the surface of our substrata were measured by a radioimmunoassay as described previously (Pelham and Wang, 1997). Briefly, the surface was reacted with primary antibodies against the coated protein, then with an iodinated secondary antibody. The gel was then peeled off the coverslip with a razor blade and counted for radioactivity. The amount of conjugated collagen was not affected by the rigidity of the substratum (determined by percentage of BIS). The amount of collagen on substrata remained unchanged for 24 h after cell plating.

Calculation of traction images

Once the substratum was manufactured and characterized, the essential experimental steps for imaging cell generated tractions were as follows: 1) cells were allowed to adhere, spread, and/or locomote on the substratum. The traction stresses generated by the cells were transmitted to the sub-

stratum, causing small movements of the marker beads. 2) A field of interest was selected and a digital image of the field was recorded using simultaneous phase and epifluorescence optics (see above). 3) Cell-substratum adhesive contacts were disrupted by treatment with trypsin. The elastic strain energy in the substratum was thereby released and the beads recoiled to their undisturbed positions. 4) Without moving the microscope stage a second digital image was recorded. 5) After registering the first and second images, the in-plane projection of the displacement vector of each bead relative to its undisturbed position was computed. Displacements of the beads in the dimension normal to the surface of the substratum also occurred, but recording these displacements was not necessary in the current application (see below). The essential data for computation are the initial marker positions, the in-plane marker displacements, and the boundaries of the cell.

Because of the finite depth of field, it is possible to simultaneously visualize the ventral portions of the cell with phase optics, and the markers located within a shallow depth of the underlying material with fluorescence optics. Thus, for the microscope used in the present study, the generic form of the marker position can be expressed as $\mathbf{m}_p = (m_{p1}, m_{p2}, \epsilon_p)$ where $p = 1, 2 \ldots N_p$ and ϵ_p has a uniform distribution in the interval between 0 and -2.5 μm. Tractions are exerted by a cell only through contacts on the free surface of the substratum (i.e., at points $\mathbf{r} = (r_1, r_2, 0)$).

Since the response of the substratum is linear, the displacement of the pth marker is necessarily related to the traction field via an integral transform;

$$d_{p\alpha} = \int\int g_{\beta\alpha}(\mathbf{m}_p - \mathbf{r}) T_\beta(\mathbf{r}) dr_1 dr_2. \quad (1)$$

Here the Greek subscripts take on values 1, 2, and 3 and summation over repeated indices is implied. The nine functions $g_{\beta\alpha}(\mathbf{m} - \mathbf{r})$ (coefficients of a Green's tensor) give the displacement of the substratum in the direction α at location $\mathbf{m}$ induced by a concentrated force in the direction β acting at location $\mathbf{r}$.

The 70-μm thickness of our fibroblast substrata is effectively infinite compared with the maximum marker displacement ($\sim$1 μm). As a result, an accurate approximation for the $g_{\alpha\beta}$ of Eq. 1 can be derived from the theory of Boussinesq for the elastic solid in the half-space underneath the cell (see Appendix A). In addition, it turns out that at or near the surface of an incompressible substratum the Boussinesq theory predicts negligible coupling of in-plane displacements to out-of-plane tractions, (i.e., $g_{13} = g_{23} = 0$). As a result, the tangent projection of marker displacement as measured in our experiments, (d_1, d_2), is a function of the tangent projection of the traction field (T_1, T_2) only. This is why observations of the normal component of bead displacement are not needed for successful numerical deconvolution of Eq. 1.

The Green's tensor appropriate for fibroblast substrata differs from the tensor used in previous work involving thin liquid-supported silicone films (Dembo et al., 1996). Otherwise, however, similar calculations are involved in producing a traction image from displacement data regardless of the type of substratum. In essence, the projected area of the cell is divided into quadrilaterals using a paving algorithm. The values of the x and y components of the traction at each node of this mesh are then determined by maximizing the total Bayesian likelihood of the predicted marker displacements (Bernardo and Smith, 1994). Complete specifics of the imaging calculation are given in Appendix B.

RESULTS

Cell behavior and morphology on soft substrata

Collagen-coated polyacrylamide substrata of several degrees of flexibility were prepared as described in the Methods section (see also Pelham and Wang, 1997). On all these substrata cells were observed to adhere, locomote, and divide. On very rigid substrata (e.g., those with 0.25% bis-acrylamide) the detailed behavior, morphology, and growth of the 3T3 cells could not be distinguished from the corresponding behavior on glass or plastic surfaces.

On the soft substrata necessary for traction imaging, 3T3 cells had very few large stress fibers and, as a population, they became more motile and more highly polarized (see Pelham and Wang, 1997). So-called "hand mirror" cells having elongated tail and a single advancing margin constituted 67% of the total as compared with 47% on hard surfaces. Average translocation of the center of the nucleus over a 1-min interval was 0.55 μm/min versus 0.05 μm/min. Ruffling activity and protrusion-retraction cycles of the leading edge were vigorous, but not unusually so. Since the surface density of type I collagen was the same for both soft and hard substrata, it was concluded that 3T3 cells are sensitive to substratum stiffness and that they respond to changes in this parameter with some characteristic alterations of morphology and behavior.

Steps in generation of a traction image

Fig. 1 *A* shows the traced outline of a polarized 3T3 fibroblast locomoting in a rectilinear fashion on our softest

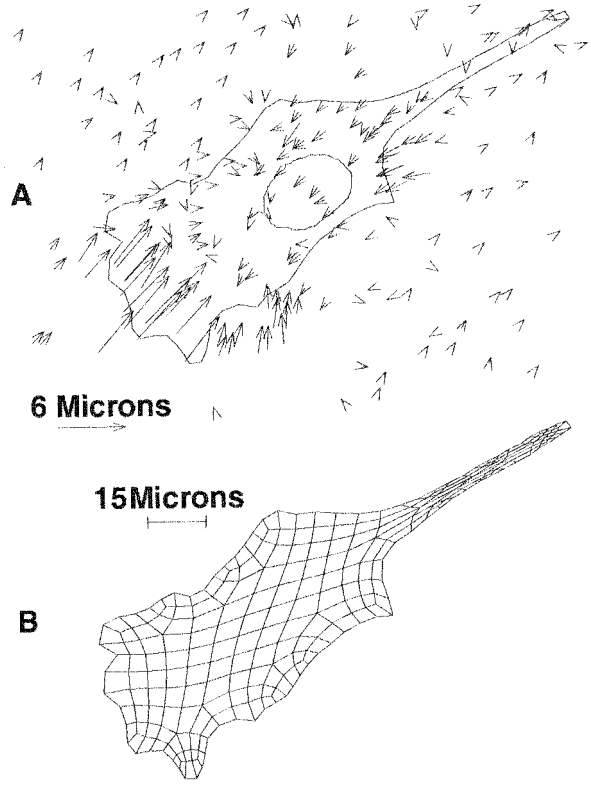

FIGURE 1 Stages in the creation of a traction image from bead displacement data. Digitized images of beads embedded in the substratum are recorded both in the presence and absence of a cell (8 bits per pixel, 512 by 384 pixels per image, 0.303 μm per pixel). (*A*) Displacement vectors (three times actual size). These start from the position of marker beads in the absence of the cell and point toward the corresponding position in the presence of the cell. These are superimposed on a tracing of the cell nucleus and of the lateral cell boundary. (*B*) A mesh is generated to pave the projected area of the cell with quadrilaterals.

fibroblast substratum (0.03% bis-acrylamide). Also indicated is the digitized outline of the cell nucleus and the observed bead displacement field. Each arrow starts at the position of a marker centroid in the absence of the cell and points toward the position when the cell is present. For better visibility, the length of the displacement vectors has been magnified by a factor of three relative to the scale used for the cell boundary (see scale vector).

Fig. 1 *B* shows a typical mesh generated by our tiling algorithm to pixilate regions of cell-substratum contact. Mesh architecture can be a limiting factor in image resolution if the spacing of quadrilaterals is insufficient to resolve all the information present in the displacement data. However, as the number of quadrilaterals is increased one reaches a point when the results are no longer dependent on the details of the mesh. By successive refinements we estimate the spacial resolution of our traction images to be $\sim 5\ \mu$m.

Fig. 2 *A* shows the maximum-likelihood traction image computed from the data of Fig. 1 *A* using the mesh of Fig. 1 *B*. The image is represented by drawing a small arrow with its base at the center of each mesh quadrilateral. This arrow has the direction of the best-fit traction vector and a length proportional to the magnitude of the traction. Finally, Fig. 2 *B* shows particle displacements as predicted from the best-fit traction field by back-substitution into Eq. 1. It agrees very well with the experimental data shown in Fig. 1 *A*.

In producing the traction image of Fig. 2 *A* we have included the best-fit vectors at the center of *all* mesh elements. This rendering is useful for some purposes but fails to represent the experimental uncertainty of the component vectors. Such uncertainty can be estimated by bootstrap computations and represented by a confidence circle (Dembo et al., 1996). The radius of this circle is almost the same for all the vectors of the image and, in the case of Fig. 2 *A*, has a value of ~ 0.5 kdyn/cm^2 ($= 50$ pN/μm^2).

Because the errors of the traction image are spatially uniform and directionally isotropic, they are analogous to the background noise of an optical image. Thus, one may graphically account for such errors simply by excluding elements that fail to pass a certain threshold from the final image. Fig. 3 shows the result of applying such a background rejection to the maximum likelihood image of Fig. 2 *A*. Additional traction images of locomoting "hand mirror" fibroblasts are shown in Figs. 4 and 5.

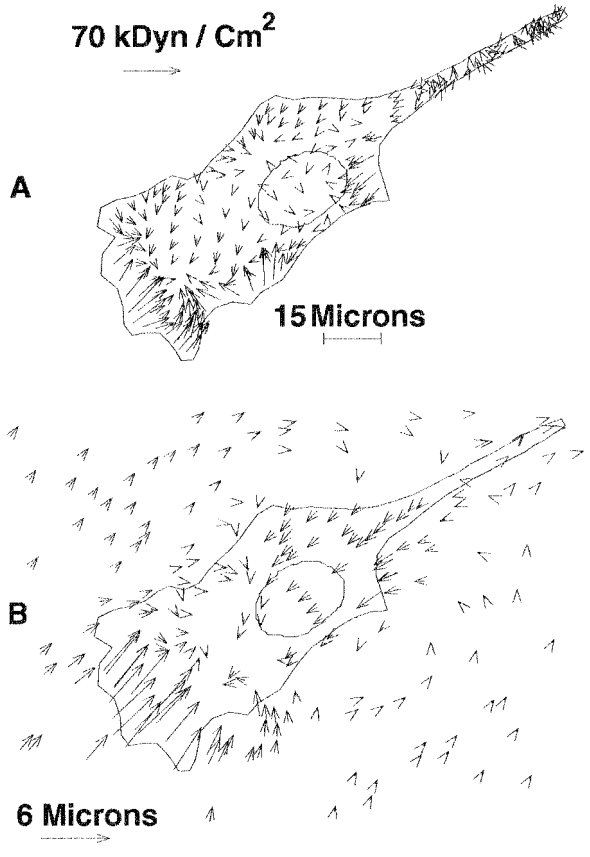

FIGURE 2 (*A*) Traction vectors that maximize Bayesian likelihood are computed and an image is rendered by drawing a vector in the center of each mesh quadrilateral. The arrowhead is of standard size but the shaft is proportional to the traction magnitude. (*B*) The theoretical marker displacements computed by back substitution of the best fit tractions into Eq. 1.

Tractions in the anterior region

The most striking feature of the images in Figs. 3–5 is a band of intense stress located within a broad swath along the edge of the anterior region. While this domain is easily recognizable in all images, there are significant variations in the magnitude of the stress within its boundaries. For example, in some cases portions of the leading edge do not seem to produce tractions at all, and in other cases short stretches of quiescent boundary break the anterior traction

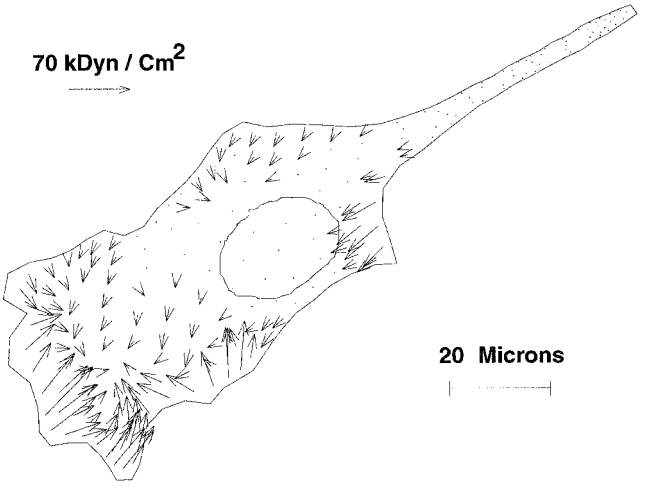

FIGURE 3 In this rendering, tractions are regarded as "significant" only if the vector magnitude is larger than its standard deviation (as computed by the bootstrap method). Sites at which the best fit traction fails to meet this significance test are represented by a small dot. Same cell as in Fig. 1. Number of marker observations, 198; RMS bead displacement, 1.72 μm; number of quadrilaterals in mesh, 215; cell area, 3148 μm^2; RMS traction stress, 16.5 kdyn/cm^2; propulsive thrust, 0.15 dyn.

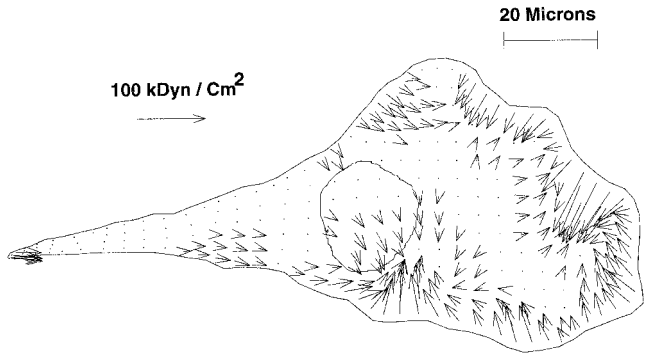

FIGURE 4 A second example of the traction image produced by a locomoting "hand mirror" fibroblast. Number of marker observations, 173; RMS bead displacement, 2.63 μm; number of quadrilaterals in mesh, 292; area of cell-substratum contact, 3883 μm^2; RMS traction stress, 24.8 kdyn/cm^2; propulsive thrust, 0.21 dyn.

zone into segments. The video record just before trypsinization reveals that the zone of anterior tractions is always coincident with loci of active ruffling activity (Abercrombie et al., 1970a, b).

In most cells the swath of strong tractions is not simply restricted to the leading edge, but extends for some distance along the lateral sides of the lamella where they become perpendicular to the anterior-posterior axis of the cell (for example see the lower edge of the cell in Fig. 3. Thus, as a general rule, tractions along the periphery of the frontal zone are largely parallel to the inward normal of the local contour, and there is no evidence that the frontal tractions are organized by the anterior-posterior axis of the cell. We should emphasize the centripetal orientation rule does *not* prove that the centripetal direction determines the traction direction. In fact, it seems equally probable that the reverse is true. A definitive answer as to cause and effect will require detailed temporal analysis.

To further reveal the nature of the traction stresses produced by the leading lamella we choose some random

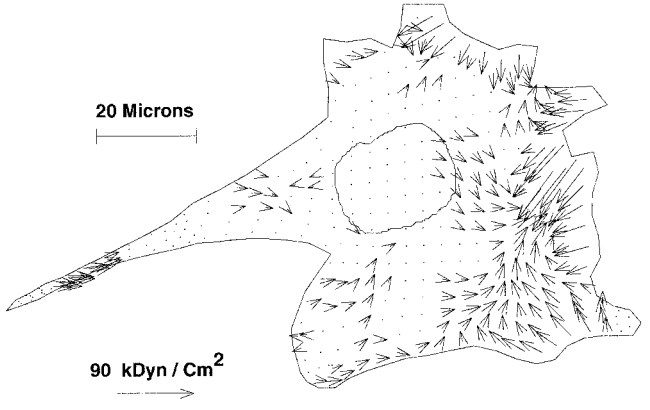

FIGURE 5 A third traction image. Number of marker observations, 166; RMS bead displacement, 1.53 μm; number of quadrilaterals in mesh, 358; cell area, 3872 μm^2; RMS traction stress, 13.2 kdyn/cm^2; propulsive thrust, 0.14 dyn.

points on the edge and follow the variations of stress along a straight inward-cutting path (Fig. 6 *A*). The direction of this path is chosen so as to coincide with that of the traction vector precisely at the cell edge. Following such a path, the centripetal stress is found to decline monotonically from its maximum value of $\sim$100 kdyn/cm^2 ($= 10^4$ pN/μm^2). Eventually this traction component reaches zero and, proceeding even further inward, it becomes increasingly negative. Thus, while the traction zones along the rim of the fibroblast lamella transmit centripetal force to the substratum, the subjacent inner portions of the lamella do the exact opposite. The opposing blocks of centripetal and centrifugal stress meet along a tectonic boundary $\sim$15 μm behind the outer edge of the cell (Fig. 6 *A*).

Tractions in the posterior region

Steadily locomoting fibroblasts typically have a long tail or uroid process that tends to be slowly extracted from the cell body and that remains fixed on the substratum as the latter moves forward (Chen, 1981). At the base of the tail the diameter of the cell swells dramatically as though to encompass the nucleus. For the subsequent discussion the tail together with the two "wings" of cytoplasm on either side and to the rear of the nucleus are regarded as comprising the posterior zone of the fibroblast.

In marked contrast with the strong localized tractions of the lamellipodium, the tractions in the posterior zone are weak and without consistent distribution. In fact we have difficulty accurately measuring posterior tractions except in a few "hot spots." For example, in Fig. 4 we can find such spots at the very tip of the tail, at the base of the tail, and in the wings on either side of the nucleus. In Fig. 5 we see a patch of traction midway along the tail, at the base of the tail, and in the wings. In Fig. 3 we detect significant traction only in the wings, not under the tail itself. From the random scatter of these sites one may surmise that subthreshold stresses of a similar nature are distributed throughout the posterior.

Unlike tractions in the anterior region, those in the posterior do not seem to dance in close partnership with the local contours of the cell. Rather, they seem to be mainly parallel to the overall vector of cell locomotion (this is particularly evident in the tail itself). Two profiles of posterior tractions are given in Fig. 6 *B*. Evidently the tractions decline with distance from the edge but they lack the distinct subjacent layer of counter-stress typical of the frontal tractions (Fig. 6 *A*).

DISCUSSION

The use of elastic substrata to produce traction images is a new technology, rapidly developing in sophistication. Here we have attempted to provide a simple benchmark by characterizing the traction images of polarized, steadily locomoting 3T3 fibroblasts on soft polyacrylamide substrata

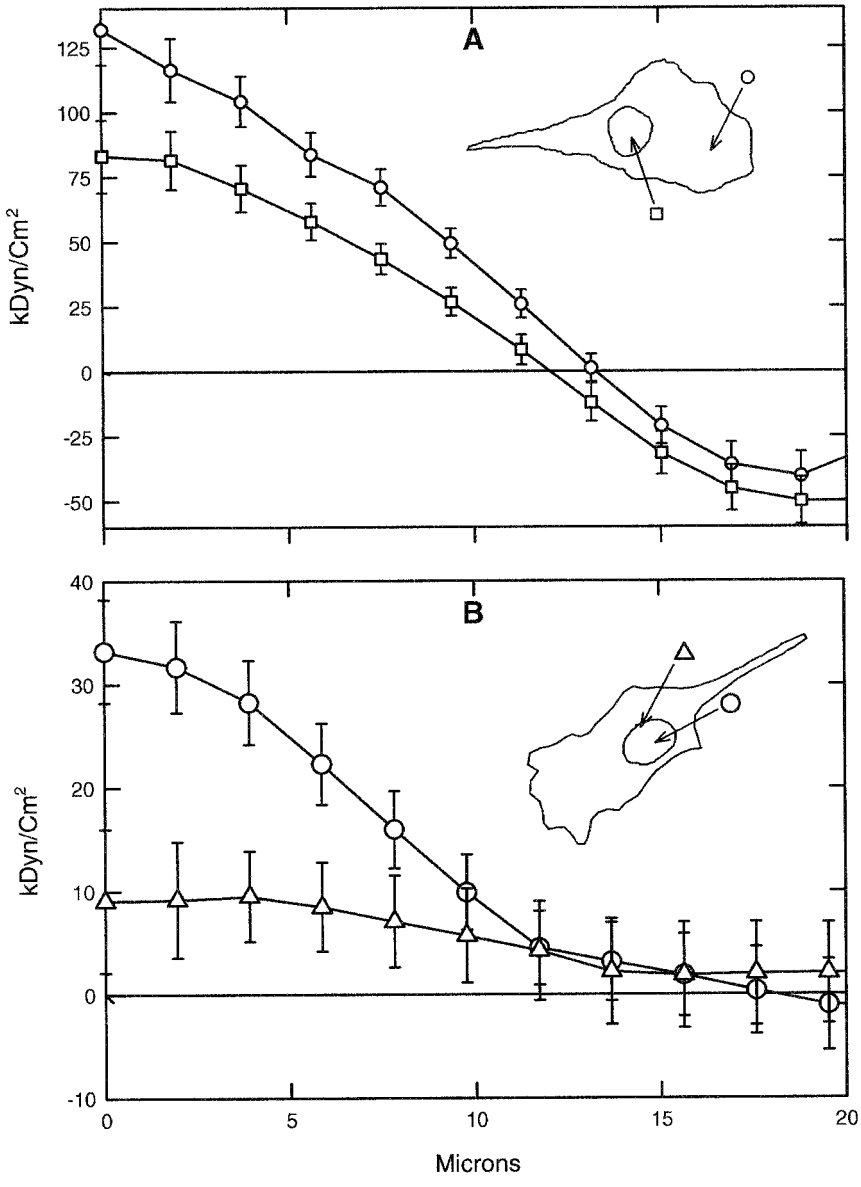

FIGURE 6 Traction along several straight paths starting at the cell edge and moving inward. In all cases the direction is chosen so as to coincide with the outermost traction vector. Error bars represent standard deviation of the traction computed with the bootstrap method. (*A*) Two paths cutting from the leading edge (same cell as in Fig. 4). Note that the centripetal traction crosses zero at a point ~15 μm inward from the edge. Proceeding further inward, the traction becomes negative (i.e., the cell is pushing the substratum outward). The lamellipodial and medullary domains of the lamella are thus characterized by opposing blocks of stress. (*B*) Two paths cutting the trailing edge (same cell as in Fig. 3). Note that the tractions along paths cutting the trailing edge lack the subjacent countertractions typically observed in the case of the frontal tractions.

(Young's modulus = 62 ± 1 kdyn/cm^2). These are the first such images to be obtained for a mammalian cell line. The conditions we have employed in this study are designed to be as close to the "physiological" conditions as possible. However, when interpreting our results it must be remembered that changes in culture conditions could well have very important consequences on cellular tractions. In particular, 3T3 cells are sensitive to the softness of the substratum (they develop fewer large stress fibers and become more polarized and more motile). Thus the tractions produced by 3T3 cells on our relatively soft substrata may be different from the tractions that would be exerted on hard surfaces even if these are of identical chemistry.

Under the conditions of our study we find that the average of the stress magnitude over the entire projected area under a cell is ~20 kdyn/cm^2 (2000 pN/μm^2). The total propulsive thrust exerted to sustain forward locomotion is calculated by projecting the stress vectors onto the long axis of the cell and summing over those regions where the force is greater than zero. The result is ~0.2 dyn (= 2×10^6 pN). In addition we find that the traction field at the front of these cells is directed centripetally along the normal of the cell edge. This frontal force field is intense (average magnitude on the order of 60 kdyn/cm^2) but is confined to a thin rim only 15 μm in width, in a region roughly coincident with the lamellipodium. Subjacent to this zone is a region of weak, more diffuse countertraction.

Two recent studies have implicated myosin II as the molecular motor ultimately responsible for the production of traction forces in 3T3 fibroblasts (Chrzanowska-Wodnicka and Burridge, 1996; Pelham and Wang, submitted for publication). If this is granted, then the magnitude of the frontal tractions we have observed, averaging 60 kdyn/cm^2, indicates that at any moment in time, the force of several

thousand myosin heads must be concentrated on each square micron of the lamellipodium-substrate interface (this assumes that each head generates a few piconewtons of force).

In assessing the implications of such remarkable force densities it should be remembered that the tractions at the leading edge are exceptional and that the area involved is small. It should also be remembered that the cytoskeleton probably possesses mechanisms capable of mechanically leveraging and focusing the elementary forces generated by myosin molecules. Finally, it is interesting that the anterior edge of the 3T3 cells does not contain a noticeable elevated concentration of myosin II (Pelham and Wang, submitted for publication). It does, however, show a continuous assembly of myosin minifilaments and ribbons that then become distributed throughout the lamella (McKenna et al., 1989; Verkhovsky and Borisy, 1993). It is therefore probable that the formation and integration of high-order myosin structures is coupled to the generation of forces.

Our observation of converging stress fields at the junction of the lamella and the lamellipodium indicates that much of the mechanical work underlying cell locomotion is generated at or near this boundary. Modularity of the contractile activity on different segments of the anterior boundary is indicated by the close correlation of the direction of the anterior traction field with the inward normal of the actively changing contour. Modularity of the contractile activity in small subdomains of the leading edge is also supported by the rapid circumferential fluctuations of the magnitude of the anterior forces and by the known statistical independence of protrusion/withdrawal cycles at positions separated by as little as 6 μm (Abercrombie et al., 1970a, b).

The observation of strong centripetal tractions under the lamellipodium indicates that this organelle has specialized grappling sites, which mechanically connect the substratum to the cytoskeleton and hence to the contractile machinery. Most likely these grappling sites correspond to either focal adhesions or the smaller, vinculin-rich focal complexes that have been reported under the lamellipodia (Nobes and Hall, 1995; Machesky and Hall, 1997). This would imply that some subset of the lamellipodial actin filaments act like tension-bearing ropes stretched between the grappling sites and the sites of force generation. The grappling line idea would seem to offer some internally consistent explanation for the well-known kinematics and morphology of the ruffling phenomenon (Abercrombie et al., 1970a, b). Clearly, if a segment of the leading edge were to lose adhesive contact with the substratum then the grappling tension might well be converted into an upward pivoting.

Because the contact sites remain fixed on the substratum during cell locomotion, new frontal adhesions as well as new connecting ropes must be continuously produced (Wang, 1985). Thus a picture emerges in which the lamellipodium is like an assembly line (Small et al., 1998). Near the front, new actin filaments and focal adhesions are produced. Further back they are joined together. Then further back still the filaments become linked to force generating molecules, and so forth. A question remains as to how the leading edge is protruded outward. Possibly this occurs simply as a result of pressure and cytosolic flow. It also seems possible that energy released during polymerization of actin filaments could be directly harnessed for production of protrusive force.

Cramer et al. (1997) have demonstrated that some actin filaments of the locomoting fibroblasts have graded polarity with barbed ends pointing forward in the lamellipodium, backward in the tail, and with mixed polarity in the lamella and cell body. In view of the standard sliding filament model, this pattern would seem to be consistent with the idea that filaments in the lamellipodium are acting as grappling lines placed under tension by contractions occurring further back. Cramer et al. also demonstrate that retrograde flow of actin occurs only in the lamellipodium and that the filaments elsewhere are either forward-moving or stationary relative to the substratum. These kinematics can be rationalized with the grappling-line idea if one supposes that the retrograde flow is restricted to dorsal filaments that fail to link with adhesion molecules. Instead of developing tension such filaments would be pulled backward.

In the posterior portion of a locomoting fibroblast we find that the traction field tends to be weak except for isolated patches. In the tail itself, and to some extent in the wings, forces are oriented parallel to the long axis, without subjacent countertractions similar to those found behind the leading edge. These properties are most consistent with the idea of friction caused by the passive stretching of stationary adhesive linkages as the cell moves forward. We do not see any firm suggestion of contractile activity in the tail (though this is not completely excluded). The marked difference in the anterior/posterior traction field indicates a corresponding differential in the density of adhesive bonds or in the mechanical susceptibility of such bonds (Schmidt et al., 1993).

Harris et al. (1980) reported studies of primary chick fibroblasts using wrinkling silicone rubber substrata (these cells are similar to 3T3 cells in motile behavior and appearance). They observed a large "compression" wrinkle at the junction of the lamella and lamellipodium (between 5 and 25 μm behind the leading edge). They also observed a series of smaller wrinkles parallel to the primary wrinkle, but further back. In addition they saw "stretch" wrinkles radiating outward from the leading edge. Complex wrinkle patterns of this sort are difficult to interpret with certainty. The authors themselves postulated that the lamellipodium was not in contact with the substratum. Nevertheless, the large wrinkle at the lamella-lamellipodium junction would seem to be consistent with our present observation of a pinching pattern of tractions at the same location.

Galbraith and Sheetz (1997) have recently reexamined the stresses produced by primary chick fibroblasts using a buried silicone cantilever. The stress magnitudes recorded by this method are quite close to those we observe. However, Galbraith and Sheetz find a complete absence of traction stress associated with the lamellipodium. Instead,

they report that the main rearward tractions come from the central portion of the lamella (behind the lamellipodium but in front of the nucleus). In addition, they find that the traction stresses at the tail of the chick fibroblasts are much stronger than those at the anterior. These observations are at variance with our present findings. We must emphasize, however, that there are many possible biological explanations for such apparent discrepancies. For example, they could be caused by differences in cell type or differences in the surface chemistry or stiffness of the substratum.

Another cell where some spatially resolved traction data are available is the fish keratocyte. The average magnitude of the interfacial stress field produced by these cells is an order of magnitude smaller than that of the 3T3 fibroblast (Dembo et al., 1996). In addition, the stress distribution in the keratocyte is best described as a transverse pinching pattern in which the lateral wings of the lamellium pull the substratum inward toward the nucleus (Lee et al., 1994; Oliver et al., 1995; Dembo et al., 1996). Centripetal tractions at the leading edge are not detectable and friction at the trailing edge is also very low (at least in normal cells).

Taken together, our observations indicate that traction is integral to the mechanism of fibroblast locomotion and that the mechanical energy for traction is derived from cytoskeletal contractile activity. It is difficult to reconcile this with models of motility that discount the centrality of contractile forces (e.g., models based on gel swelling, osmotic pressure, or Brownian ratchets). Contrary to previous indications (Galbraith and Sheetz 1997; Harris et al., 1980), we find that the advancing edge of a fibroblast is quite capable of transmitting force to the substratum. In fact, we find that the entire force for propulsion is exerted at this edge and that these forces are independently modulated at high frequency. The junction of the lamella and the lamellipodium seems to be the location of the most intense contractions. The midbody and posterior are apparently passive structures being pulled forward by these contractions like the cars of a freight train. This apparently excludes any model placing the main contractile engine in the posterior portion of the cell (i.e., tail contraction models). Also excluded are any models in which contraction is not directly coupled to the lamellipodium. For example, retraction fibers cannot be the primary contractile engines because these fibers connect the cytoskeleton of the cell body and posterior to large focal adhesions located under the lamella.

Beyond these indications, the overall pattern of traction stress exerted by 3T3 cells can be rationalized in terms of a mechanism of locomotion proposed some time ago by DiMilla et al. (1991). The essential idea is that adhesions in the tail of the cell are intrinsically weaker than those in the front. Contraction of the cytoskeleton causes tension to be conducted to these two classes of adhesions, pulling the frontal adhesions backward and pushing the tail adhesions forward. Because of their relative weakness, the bonds at the trailing edge are the first to give way, causing both cytosolic flow and frontal membrane protrusion. The cycle is completed with the formation of new adhesions and cytoskeleton at the leading edge. Other evidence relevant to the DiMilla model has been discussed in several recent reviews (e.g., Lauffenburger and Horwitz, 1996; Sheetz, 1994; Sheetz et al., 1998).

APPENDIX A

The Boussinesq equations

Let $\mathbf{x} = (x_1, x_2, x_3)$ be a Cartesian position vector, let the distance from the origin be $r \equiv (x_1^2 + x_2^2 + x_3^2)^{1/2}$, and let the half-space $x_3 \leq 0$ contain an elastic solid characterized by Young's modulus E and Poisson ratio v. For each position in the material $g_{\beta\alpha}(\mathbf{x})$ represents the α-displacement caused by a concentrated unit force exerted at the origin of coordinates in the β-direction. We reproduce below the formulas for these functions due to Boussinesq (the derivation is given in Section 1.8 of Landau and Lifshitz, 1986).

$$g_{11} = \frac{1+v}{2\pi E}\left(\frac{(2(1-v)r - x_3)}{r(r-x_3)} + \frac{(2r(vr-x_3)+x_3^2)x_1^2}{r^3(r-x_3)^2}\right)$$

$$g_{21} = \frac{1+v}{2\pi E}\left(\frac{(2r(vr-x_3)+x_3^2)x_1x_2}{r^3(r-x_3)^2}\right)$$

$$g_{31} = \frac{1+v}{2\pi E}\left(\frac{x_1x_3}{r^3} + \frac{(1-2v)x_1}{r(r-x_3)}\right)$$

$$g_{12} = \frac{1+v}{2\pi E}\left(\frac{(2r(vr-x_3)+x_3^2)x_1x_2}{r^3(r-x_3)^2}\right)$$

$$g_{22} = \frac{1+v}{2\pi E}\left(\frac{(2(1-v)r - x_3)}{r(r-x_3)} + \frac{(2r(vr-x_3)+x_3^2)x_2^2}{r^3(r-x_3)^2}\right)$$

$$g_{32} = \frac{1+v}{2\pi E}\left(\frac{x_2x_3}{r^3} + \frac{(1-2v)x_2}{r(r-x_3)}\right)$$

$$g_{13} = \frac{1+v}{2\pi E}\left(\frac{x_1x_3}{r^3} - \frac{(1-2v)x_1}{r(r-x_3)}\right)$$

$$g_{23} = \frac{1+v}{2\pi E}\left(\frac{x_2x_3}{r^3} - \frac{(1-2v)x_2}{r(r-x_3)}\right)$$

$$g_{33} = \frac{1+v}{2\pi E}\left(\frac{2(1-v)}{r} + \frac{x_3^2}{r^3}\right)$$

Note that the g_{ij} have units of displacement per unit force and that in general $g_{ij} \neq g_{ji}$. Also observe that the second subscript gives the component of the displacement and the first gives the component of force. Note also that since the substratum is in the lower half-space, surface forces that press into the material along the O3 axis have a negative sign, whereas tractions that pull the material upward have a positive sign.

APPENDIX B

Mathematical details

Our purpose here is to describe the precise definitions of complexity and likelihood used for generating the fibroblast traction images in this study. The basic ideas were originally introduced in the context of images based on silicone substrata by Dembo et al. (1996) but we have since made some minor improvements.

The mesh

The first step of an imaging computation is to introduce a quadrilateral mesh so as to tessellate and define the allowed domain of the traction field. Within this domain the in-plane traction components are then approximated by functions of the type

$$T_\beta(\mathbf{r}) \approx T_{k\beta} H_k(\mathbf{r}) \tag{B1}$$

where the $H_k(\mathbf{r})$ are standard bilinear shape functions and the $T_{k\beta}$ are the components of the nodal traction vectors. The summation in Eq. B1 is intended to extend over all the nodes of the mesh (i.e., $k = 1, 2, \ldots N_n$).

The chi-square statistic

For a given mesh any choice of the $T_{k\beta}$ corresponds to an allowable traction image. Substitution of Eq. B1 into Eq. 1 of the main text demonstrates that any such image makes a definite prediction about the marker displacements

$$d_{p\alpha} = d_\alpha(\mathbf{m}_p) = T_{k\beta} \int\int g_{\alpha\beta}(\mathbf{m}_p - \mathbf{r}) H_k(\mathbf{r}) dr_1 dr_2$$

$$= A_{k\beta p\alpha} T_{k\beta}. \tag{B2}$$

Note that the $A_{k\beta p\alpha}$ depend only on mesh geometry, the bead locations, and the material properties of the substratum, and that the index p runs over the markers (i.e., $p = 1, 2, \ldots N_p$). Once these matrix elements have been computed, the ability of some particular traction image to explain the displacement observations can be quickly and objectively measured by means of the familiar "chi-square" statistic

$$\chi^2 \equiv (\hat{d}_{p\alpha} - d_{p\alpha})^2 \sigma_{p\alpha}^{-2} \tag{B3}$$

$$= (\hat{d}_{p\alpha} - A_{k\beta p\alpha} T_{k\beta})^2 \sigma_{p\alpha}^{-2}. \tag{1}$$

Here $\hat{d}_{p\alpha}$ is the *experimental* displacement of the pth marker particle along the α-coordinate axis, $\sigma_{p\alpha}$ is the error of $\hat{d}_{p\alpha}$, and summation over all repeated indices is implied.

The information statistic

The intrinsic "complexity" of a traction image also needs to be objectively quantified. For a vector image, this is conveniently accomplished by the following scalar invariant (Dembo et al., 1996)

$$\mathscr{C}^2 \equiv \int_\Omega (\partial_\alpha T_\beta + \partial_\beta T_\alpha)(\partial_\alpha T_\beta + \partial_\beta T_\alpha) dr_1 dr_2. \tag{B4}$$

As in the case of χ^2, substitution of Eq. B1 and term-by-term integration allows the complexity of a traction image to be written as a quadratic form in the nodal degrees of freedom

$$\mathscr{C}^2 = C_{i\alpha j\beta} T_{i\alpha} T_{j\beta}. \tag{B5}$$

Note that the $C_{i\alpha j\beta}$ are constants that depend only on mesh geometry.

The Bayesian likelihood

Combining Eqs. B3 and B5 the Bayesian likelihood of the $T_{k\beta}$ is

$$L_b(T_{k\beta} | \hat{d}_{p\alpha}) = \exp[-(\chi^2 + \lambda \mathscr{C}^2)], \tag{B6}$$

where λ is a positive real number that needs to be determined by the criterion of maximum entropy (i.e., to obtain the simplest image consistent with a given data set).

Maximizing entropy

For any given choice of the quantity λ, the maximum likelihood nodal tractions can be determined by minimizing the linear combination $\chi^2 + \lambda \mathscr{C}^2$ (this is simply a matter of solving a linear system). The values of χ^2 and $\mathscr{C}^2$ obtained by substitution of such maximum likelihood tractions into Eqs. B3 and B5 are then denoted $\bar{\chi}^2$ and $\bar{\mathscr{C}}^2$, respectively. If calculations are carried out for a series of increasing values of λ, then the resulting $\bar{\chi}^2$ and the $\bar{\mathscr{C}}^2$ values will be an increasing and decreasing series, respectively. Starting with $\lambda = 0$ and progressively increasing this quantity, one therefore eventually reaches a point at which $\bar{\chi}^2$ becomes unacceptable (as in the usual chi square test it is conventional to say that an image is unacceptable if $\bar{\chi}^2 \gtrapprox N_p + \sqrt{N_p}$). The threshold image with $\bar{\chi}^2 \approx N_p + \sqrt{N_p}$ is then the simplest traction distribution consistent with the given experimental data.

Global force and torque balances

When measuring displacements, errors in the registry of the first and second images can result in small rotational and translational errors that apply equally to all markers. For a given particle distribution, a given mesh, and a given value of λ, the traction modes resulting from each mechanism of rigid-body substratum displacement were computed in a separate calculation and stored. Then a linear combination of these three modes was subtracted from the threshold image, the amplitudes being chosen to enforce global torque balance and global balance of the two Cartesian components of force. In previous work with silicone substrata drift corrections of this sort were sometimes quite important for correcting small artifacts in the traction images. However, in the present studies we never found any visible difference in images before and after drift correction. This stability against drift is an important advantage of polyacrylamide substrata.

Analysis of error

After completion of the drift corrections, it is still necessary to test the various vectors of the final traction image for statistical significance. This is done by bootstrap analysis (Efron and Tibshirani, 1986). Essentially, such analysis involves adding random noise to the maximum likelihood displacements, recomputing an image using the simulated data, logging this modified image, and repeating for several cycles. The detailed methodology of such bootstrap calculations, and also Monte Carlo trials of overall performance, have been described elsewhere (Dembo et al., 1996).

The authors thank Robert Pelham for technical assistance.

This research was supported by National Institutes of Health Grants AI21002 (to M.D.) and GM32476 (to Y.W.). The contents of this article are solely the responsibility of the authors.

REFERENCES

Abercrombie, M., J. E. M. Heaysman, and S. M. Pegrum. 1970a. The locomotion of fibroblasts in culture. I. Movements of the leading edge. *Exp. Cell Res.* 59:393–398.

Abercrombie, M., J. E. M. Heaysman, and S. M. Pegrum. 1970b. The locomotion of fibroblasts in culture. II. Ruffling. *Exp. Cell Res.* 60: 437–444.

Barocas, V. H., and R. T. Tranquillo. 1997. An anisotropic biphasic theory of tissue-equivalent mechanics: the interplay among cell traction, fibrillar network deformation, fibril alignment, and cell contact guidance. *J. Biomech. Eng.* 119:137–145.

Bernardo, J. M., and A. F. M. Smith. 1994. Bayesian Theory. John Wiley and Sons, Chichester, UK.

Burton, K., and D. L. Taylor. 1997. Traction forces of cytokinesis measured with optically modified substrata. *Nature.* 385:450–454.

Chen, W. T. 1981. Mechanism of retraction of the trailing edge during fibroblast movement. *J. Cell Biol.* 90:187–200.

Chen, C. S., M. Mrksich, S. Huang, G. M. Whitesides, and D. E. Ingber. 1997. Geometric control of cell life and death. *Science.* 276:1425–1428.

Chrzanowska-Wodnicka, M., and K. Burridge. 1996. Rho-stimulated contractility drives the formation of stress fibers and focal adhesions. *J. Cell Biol.* 133:1403–1415.

Condeelis, J. 1993. Life at the leading edge: the formation of cell protrusions. *Annu. Rev. Cell Biol.* 9:411–444.

Cramer, L. P., and T. J. Mitchison. 1993. Moving and stationary actin filaments are involved in spreading of postmitotic PtK3 cells. *J. Cell Biol.* 122:833–843.

Cramer, L. P., M. Siebert, and T. J. Mitchison. 1997. Identification of novel graded polarity actin filaments in locomoting heart fibroblasts: implications for the generation of motile force. *J. Cell Biol.* 136: 1287–1305.

Dembo, M., T. Oliver, A. Ishihara, and K. Jacobson. 1996. Imaging the traction stresses exerted by locomoting cells with the elastic substratum method. *Biophys. J.* 70:2008–2022.

DiMilla, P. A., K. Barbee, and D. A. Lauffenburger. 1991. Mathematical model for the effects of adhesion and mechanics on cell migration speed. *Biophys. J.* 60:15–37.

Efron, B., and R. Tibshirani. 1986. Bootstrap methods for standard errors, confidence intervals, and other measures of statistical accuracy. *Statistical Sci.* 1:54–77.

Folkman, J., and A. Moscona. 1978. Role of cell shape in growth control. *Nature.* 273:354–349.

Galbraith, C. B., and M. P. Sheetz. 1997. A micromachined device provides a new bend on fibroblast traction forces. *Proc. Natl. Acad. Sci. USA*. 94:9114–9118.

Harris, A. K. 1988. Fibroblasts and myofibroblasts. *Methods Enzymol.* 163:623–642.

Harris, A. K., P. Wild, and D. Stopak. 1980. Silicone rubber substrata: a new wrinkle in the study of cell locomotion. *Science.* 208:177–179.

Landau, L. D., and E. M. Lifshitz. 1986. Theory of Elasticity, 3rd ed. J. B. Sykes and W. H. Reid, translators. Pergamon Press, Oxford, UK.

Lauffenburger, D. A., and A. L. Horwitz. 1996. Cell migration: a physically integrated molecular process. *Cell.* 84:359–369.

Lee, J., M. Lenord, T. N. Oliver, A. Ishihara, and K. Jacobson. 1994. Traction forces generated by locomoting cells. *J. Cell Biol.* 127: 1957–1964.

Machesky, L. M., and A. Hall. 1997. Role of actin polymerization and adhesion to extracellular matrix in rac and rho-induced cytoskeletal reorganization. *J. Cell Biol.* 138:913–926.

McKenna, N. M., Y-L. Wang, and M. E. Konkel. 1989. Formation and movement of myosin-containing structures in living fibroblasts. *J. Cell Biol.* 109:1163–1172.

Nobes, C. A., and A. Hall. 1995. Rho, rac, and Cdc42 GTPases regulate the assembly of multimolecular focal complexes associated with actin stress fibers, lamellipodia, and filopodia. *Cell.* 81:53–62.

Oliver, T., M. Dembo, and K. Jacobson. 1995. Traction forces in locomoting cells. *Cell Motil. Cytoskeleton.* 31:225–240.

Oliver, T., K. Jacobson, and M. Dembo. 1998. Design and use of substrata to measure traction forces exerted by cultured cells. *Methods Enzymol.* 298:497–488.

Oliver, T., J. Lee, and K. Jacobson. 1994. Forces exerted by locomoting cells. *Seminars Cell Biol.* 5:139–147.

Pelham, R. J., and Y-L. Wang. 1997. Cell locomotion and focal adhesions are regulated by substrate flexibility. *Proc. Natl. Acad. Sci. USA*. 94: 13661–13665.

Schmidt, C. E., A. F. Horwitz, D. A. Lauffenburger, and M. P. Sheetz. 1993. Integrin-cytoskeletal interactions in migrating fibroblasts are dynamic, asymmetric, and regulated. *J. Cell Biol.* 123:977–991.

Sheetz, M. P. 1994. Cell migration by graded attachment to substrates and contraction. *Seminars Cell Biol.* 5:149–155.

Sheetz, M. P., D. P. Felsenfeld, and C. G. Galbraith. 1998. Cell migration: regulation of force on extracellular matrix-integrin complexes. *Trends Cell Biol.* 8:51–54.

Small, J. V., K. Rottner, I. Kaverina, and K. I. Anderson. 1998. Assembling an actin cytoskeleton for cell attachment and movement. *Biochim. Biophys. Acta.*, in press.

Verkhovsky, A. B., and G. G. Borisy. 1993. Non-sarcomeric mode of myosin II organization in fibroblast lamellum. *J. Cell Biol.* 123: 637–652.

Wang, Y-L. 1985. Exchange of actin subunits at the leading edge of living fibroblasts: possible role of treadmilling. *J. Cell Biol.* 101:597–602.

Wang, Y-L., and R. J. Pelham, Jr. 1998. Preparation of a flexible, porous polyacrylamide substrate for mechanical studies of cultured cells. *Methods Enzymol.* 298:489–496.